Journal of Materials Chemistry A

ROYAL SOCIETY OF CHEMISTRY

PAPER

View Article Online
View Journal | View Issue

Cite this: J. Mater. Chem. A, 2023, 11, 717

Enabling technologies for the continuous electrically driven conversion of CO_2 and water to multi-carbon products at high current densities†

Mahak Dhiman, ‡[a] Yingying Chen,‡[b] Yifei Li,[a] Anders B. Laursen,[a] Karin U. D. Calvinho, [a] Todd G. Deutsch *[b] and G. Charles Dismukes *[ac]

Herein, we demonstrate greatly improved conversion of CO_2 using a gas diffusion electrode (GDE) with flowing electrolyte configuration for CO_2 gas delivery in combination with a high surface area nickel phosphide electrocatalyst. This configuration achieves 40–50% selectivity for total carbon products over H_2 formation (HER) at total current densities ranging from 50 to 300 mA cm^{-2}. We developed a soft-templating method using CTAB detergent micelles for synthesis of phase-pure Ni_2P, achieving a 260-fold larger surface area (BET) and porous sponge-like morphology that produces stable currents. This catalyst produces mainly one C-product, methylglyoxal (MG, $C_3H_4O_2$) with 38–47% overall selectivity, the highest reported selectivity for a 12-electron reduction product. The versatile soft-templating method for electrocatalyst synthesis uses low-temperature (185 °C) that is permissive for incorporation of co-catalysts that are otherwise destroyed by the high temperatures used in traditional solid-state synthesis (SSS). The non-porous Ni_2P-SSS catalyst produces mainly H_2 at these current densities. Achieving these high currents and C/H selectivity benefits from use of hydrophobic polymers as co-catalyst binders (cationic = Nafion, anionic = PFAEM and neutral = PTFE) to improve CO_2 conversion. PFAEM is the better ionomer for the CO_2RR at high current density, postulated as due to suppressing CO_2 conversion to inactive bicarbonate. Precipitation of the carbon products as a polycarbonate polymer occurs at high currents.

Received 19th October 2022
Accepted 25th November 2022

DOI: 10.1039/d2ta08173c

rsc.li/materials-a

Introduction

Electrocatalytic reduction of carbon dioxide (CO_2RR) can currently produce simple C_1, C_2, C_3 and C_4 carbon products in small scale research reactors under benign reaction conditions. Scaling up of this technology to produce multi-carbon products is widely sought as it would help mitigate environmental and climate problems posed by steadily increasing atmospheric CO_2 caused by the use of petrochemicals and fossil fuels. The CO_2RR is a scalable carbon-negative technology when coupled with renewable electricity as the power source and abundant water as the hydrogen source.[1] However, these reactions occur in competition with the electroreduction of water to hydrogen (HER) in aqueous solutions and remains an open challenge. For many simple metal catalysts, the dominant carbon products are C_1 mixtures (*e.g.*, CO, CH_4, and CH_3OH) with electrical conversion efficiency, termed faradaic efficiency (FE), approaching 90%. These catalysts require the use of scarce noble metals: Au, Ag, Pd, *etc.*[2–5] Other noble-metal-free catalysts, *e.g.*, Cu, Ni, Sn, Bi, Co, or carbon-based materials, are important alternatives, but suffer from high overpotentials, producing a mixture of products at low current densities and with low FEs.[4,6–9] In contrast to simple elements, binary and higher-stoichiometry compounds are emerging that show major improvements in overall CO_2RR performance to multi-carbon products.[10–13] Such compounds potentially allow greater flexibility to control both the electronic degrees of freedom and the acid/base groups essential for catalysis of the various bond rearrangement steps needed to produce complex products. For example, Koper *et al.* investigated PdAu alloys for CO_2 reduction to C_1 to C_5 hydrocarbons, albeit the highest faradaic efficiency toward C_5 product was only 0.07%.[14] Sargent *et al.* also demonstrated that introducing positive valence sites in a Cu electrocatalyst *via* boron doping allowed FE for C_2 products up to 80% at current densities <100 mA cm^{-2}.[15] In an alternative approach, a FE of 62% towards various C_2 and C_3 products at a total current density of 300 mA cm^{-2} was achieved but required two-step cascade operation with the Ag catalyst first converting CO_2 to

[a]Department of Chemistry and Chemical Biology, Rutgers, The State University of New Jersey, 610 Taylor Road, Piscataway, New Jersey 08854, USA. E-mail: dismukes@rutgers.edu

[b]National Renewable Energy Laboratory, Golden, Colorado 80401, USA. E-mail: Todd.Deutsch@nrel.gov

[c]Waksman Institute of Microbiology, Rutgers, The State University of New Jersey, 190 Frelinghuysen Road, Piscataway, New Jersey, 08854, USA

† Electronic supplementary information (ESI) available. See DOI: https://doi.org/10.1039/d2ta08173c

‡ Mahak Dhiman and Yingying Chen contributed equally to this work.

CO followed by the Cu catalyst reducing CO to multi-carbon products.[16] Though such advances are continuously overcoming the present limitations, controlling the reaction selectivity to a high molecular-weight product at high current density in a single-step remains a major unsolved challenge for commercial applications.

Influenced by nature's exclusive use of Ni and group 15 conjugated ligands in the active sites of the exergonic class of CO_2-fixing enzymes found in acetogenic and methanogenic bacteria, our group adapted this chemistry to examine the nickel phosphide compounds (Ni_xP_y) as HER and CO_2RR electrocatalysts.[17–20] Among the five Ni_xP_y crystalline phases investigated so far, all react with CO_2 in water to form identical products but with different amounts: C_1 (formic acid), C_3 (methylglyoxal) or C_4 (2,3-furandiol). The relative amounts of the C_1, C_3 and C_4 products have been previously shown to form on Ni_2P and Fe_2P exclusively by the formate pathway (no CO as the intermediate).[17,18] The proposed mechanism involves two successive hydride transfers to produce formate then formaldehyde, followed by two successive aldol couplings with formaldehyde and dehydration to form methylglyoxal, followed by enolization and another aldol coupling to form 2,3-furandiol.[18] The Ni_2P and NiP_2 catalysts exhibit unprecedented FEs approaching 99% for total C-products. Although, this performance was observed at applied potentials close to the reversible hydrogen electrode (RHE) where current densities are intrinsically low, and the reactions reach a steady-state distribution of products.

The formation of surface hydrides ($*H^-$) on transition metal phosphides in water is essential to favor the formate pathway. Their chemistry has been studied both experimentally and theoretically.[17–23] Grand Canonical-DFT (GC-DFT) calculations and experiments have revealed that *formate, not *CO, is the initial intermediate that is formed from surface phosphinohydrides on Fe_2P, analogous to the mechanism on isostructural Ni_2P.[17] Additional reports have predicted surface hydride transfer steps, along with surface-mediated C–C coupling to be essential for the selectivity towards multi-carbon products on Ni_2P catalysts.[21–23]

Here we examine two strategies to increase the overall CO_2RR performance by increasing the surface density of catalytic sites (surface area) and adoption of a flow design that circulates CO_2 to the catalyst surface. We report a soft-templating (-ST) synthesis to produce high surface area Ni_2P and demonstrate its significantly improved CO_2RR performance *vs.* H_2 production, improved methylglyoxal selectivity and stable operation at commercially relevant current densities in a gas/liquid flow cell design. We compare this to a non-porous Ni_2P catalyst synthesized *via* solid state synthesis (-SSS) and demonstrate that its C/H selectivity becomes strongly limited by CO_2 mass transport with increasing current densities. We illustrate the influence on C/H product selectivity of using three distinct hydrophobic polymers to bind the Ni_2P catalyst to the cathode of a gas diffusion electrode (GDE) in a flow cell. The combination of the high surface area Ni_2P catalyst operating in a flow-cell with a GDE enables continuous production of CO_2RR products with FE up to 47% and total current densities ranging from 50 to 300 mA cm^{-2}. The selectivity on Ni_2P at these high current densities shifts to methylglyoxal as the main carbon product, offering even greater value for production of this major chemical feedstock. This 12-electron reduction product and ~24 mA cm^{-2} partial current density is, to the best of our knowledge, the highest electrochemical conversion efficiency to a C_3 product in the literature.

Experimental

Soft-templating synthesis procedure

In a typical synthesis, cetyltrimethylammonium bromide (CTAB = 1.5 g) or sodium monododecyl phosphate (SMDP = 1.5 g) was stirred (700 RPM) in a water (100 mL) and cyclohexane (100 mL) mixture. After 15 min of stirring, 1-hexanol (10 mL) was added dropwise. The resulting solution was further stirred for 30 min at room temperature followed by addition of nickel(II) chloride hexahydrate salt (10 g) and red phosphorus (12 g). The resulting solution was transferred into a Teflon-sealed autoclave reactor and was heated to 185 °C for 24 h. After completion of the reaction, the mixture was allowed to cool down to room temperature. The black solid product formed was isolated by centrifugation and unreacted species including surfactant molecules were removed by washing with water (until the supernatant is a clear solution). The isolated product was further washed with 3% HCl to remove the surface phosphate/oxide species, followed by ethanol wash in the end. The as-synthesized materials were dried at 60 °C for 6 h and termed Ni_2P-CTAB and Ni_2P-SMDP.

Solid state synthesis procedure

Nickel (Ni) metal powder was mixed with red phosphorus (P) in a mortar and pestle for 15 min and transferred to a quartz tube, then flushed with argon and evacuated to less than 100 mTorr three times. The evacuated quartz tube contained 5 grams of sample, which was sealed and heated at a rate of 0.5 °C min^{-1} stepwise (350 °C, 450 °C, and 550 °C) to 750 °C. The temperature was maintained for 6 h at each intermediate step, and 24 h at the final temperature. The as-synthesized material was termed Ni_2P-SSS.

HER measurements

All solutions were prepared using Millipore water. A three-electrode setup, with a porous glass frit separating the working and counter compartments, was used for the HER measurements. To avoid the possibility of Pt contamination during stability measurements, a B-doped diamond electrode was used as a counter electrode. $Hg/HgSO_4$ was used as the reference electrode. The working compartment was purged with 1 atm. H_2 prior to and during the measurements. All electrochemical potentials are reported *vs.* the reversible hydrogen electrode (RHE) by measuring the open circuit potential of a clean Pt electrode under 1 atm. H_2 in 0.5 M H_2SO_4.

Flow cell setup for the CO_2RR

A custom-built cathode with 25 cm^2 active area was used to evaluate the performance and durability of the electrochemical

reduction of CO_2.[24] A commercial bipolar membrane (BPM) (FBM, Fumatech GmbH, FuelCellStore) was placed right next to the Ni foam in reverse-bias mode with the cation exchange layer (CEL) and the anion exchange layer (AEL) facing the cathode and anode, respectively. A catholyte flow channel was created within the PTFE gasket measuring 1.27 mm right next to the CEL of the BPM. A cathode GDE with 25 cm^2 active area was placed against the cathode flow field sealed with PTFE gaskets and was compressed to 18% once the cell was tightened to 40 inch-pound. The endplates of the cell were heated to 60 °C and kept constant for all experiments. The flow plates for the cathode and anode were made from Ti and had a 25 cm^2 area of triple serpentine flow channels. CO_2 heated to 60 °C was delivered to the cathode GDE through the cathode flow plate at a constant flow rate of 2 NLPM. 1 M potassium hydroxide (KOH) electrolyte made by dissolving KOH pellets (certified ACS, VWR) in deionized water was heated to 60 °C and fed to the anode flow plate at 50 mL min^{-1}. 0.4 M potassium sulfate (K_2SO_4) made by dissolving K_2SO_4 (ACS reagent 99.7% Sigma Aldrich) powder in deionized water was fed to the catholyte layer at 40 mL min^{-1}.

Results and discussion

We chose the Ni_2P phase of nickel phosphides as the catalyst for this investigation as we previously found that Ni_2P-SSS exhibits a FE of 99% for the CO_2RR with the highest for methylglyoxal and 2,3-furandiol (26% and 71% at 0 V *vs.* RHE, respectively).[18] In order to produce a high surface area catalyst and a small crystallite size, we used a liquid-phase soft-templating strategy that uses surfactant molecules to control the reaction volume and morphology. These variables are controlled by selection of the surfactant packing parameter, which in turn depends upon the volume and length of the non-polar template chains and the effective area of the polar head.[25] Two -ST catalysts were prepared hydrothermally by heating nickel chloride ($NiCl_2 \cdot 6H_2O$) and red phosphorus to 185 °C for 24 hours in the microemulsion formed using either cetyltrimethylammonium bromide (CTAB) or sodium monododecyl phosphate (SMDP) as surfactant molecules, cyclohexane, 1-hexanol and water. The ratio between the surfactant and solvents was optimized such that micelles adopted the inverted structure known as the L_2 phase in the Gibb's phase diagram of CTAB/1-hexanol/water systems.[26] Formation of a lamellar micelle structure under our chosen conditions of temperature and pressure has been proposed by Monson *et al.* from molecular dynamics simulations.[27] Upon heating, nucleation of precursors occurs in the aqueous compartment of the lamellar micelle structure, and growth is confined to this space.

Scanning electron microscopy (SEM) analysis of both catalysts indicates that CTAB results in a material with interconnected pores of variable pore size from 50 nm to 150 nm, and variable pore separation from 30 nm to 200 nm (Fig. 1a). By contrast, SMDP forms irregular shaped particles with size ranging from 50 to 300 nm and a distinctive rough surface morphology (Fig. 1b). For comparison to our previous benchmark, we also synthesized Ni_2P-SSS by reacting stoichiometric amounts of red phosphorus with Ni powder at 750 °C in a vacuum (Fig. 1c). Careful control of this ratio and mixing is critical to achieving single phase purity and elimination of the unreacted material. After synthesis, the Ni_2P-SSS powder was washed with 3% HCl to remove any soluble phosphate species. Ni_2P-SSS consists of larger particles with an average size ranging from 2–6 μm, which significantly limits the effective surface area. The phase purity and crystallinity of all the Ni_2P catalysts were confirmed using powder-ray diffraction, PXRD (Fig. 1d). The major peaks at 40.6°, 44.5°, 47.2°, 54.1°, 54.9°, 66.3°, 72.6° and 74.6° corresponded to the (111), (021), (210), (300), (002), (212), (321) and (211) lattice planes, matching exactly to the Ni_2P hexagonal crystal structure (ICSD reference pattern: PDF 03-065-3544). All three Ni_2P materials (SSS, CTAB, and SMDP) are polycrystalline in nature. Ni_2P adopts an ABAB layer arrangement along the [0001] direction of the crystal structure in which the alternating layers have stoichiometric Ni_3P_2 and Ni_3P.[28] Experiments on Ni_2P single crystals[29,30] and DFT calculations,[31] indicate that the hexagonal (0001) surface is terminated with P adatoms (Ni_3P–P) that stabilize the surface bonding to three fold Ni atoms. Recent ^{31}P solid-state NMR studies, combined with HRTEM, XRD crystal structure analysis and DFT-calculations of Ni_2P nanoparticles have identified the individual crystal facets that terminate the surfaces of Ni_2P nanoparticles as the (0001) and the (10$\bar{1}$ 0) facets, with the former being the dominant terminating surface of the ultrathin nanoparticles.[32] As the nanoparticles grow in size, the (1010) facets prevail, indicating that nanoparticles grow along the [0001] zone axis, exposing predominately lateral (1010) surfaces. These studies agree with earlier first principles thermodynamic studies showing that the equilibrium morphology of Ni_2P nanoparticles and nanowires exposes predominantly the (0001)

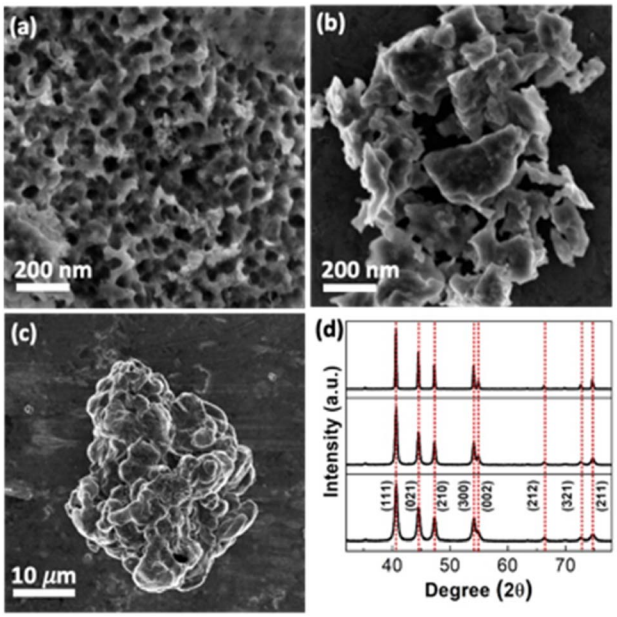

Fig. 1 (a) SEM image of Ni_2P-CTAB, (b) Ni_2P-SMDP, and (c) Ni_2P-SSS catalysts. (d) PXRD pattern of these three Ni_2P catalysts, ordered bottom to top, respectively.

Table 1 Particle size (from PXRD and SEM), N_2 gas porosity (from BET), and roughness factor of the Ni_2P catalysts

Catalyst	PXRD crystallite size from the Scherrer equation (nm)	BET surface area ($m^2\ g^{-1}$)	SEM particle size range (nm)	Roughness factor ($cm^2\ cm_{geo}^{-2}$)
Ni_2P-SSS	>50	0.1	2000–6000	220
Ni_2P-SMDP	16	5	50–400	689
Ni_2P-CTAB	12	26	30–200	720

and $(10\bar{1}0)$ facets and less frequently either the $(101\bar{1})$ or $(1\bar{1}20)$ facets, respectively.

Table 1 lists the average crystallite size as obtained from the Scherrer equation, molecular surface area as determined by cryogenic N_2 gas adsorption using the BET method, and the roughness factor as determined by dividing the ECSA by the geometric area.

Influence of surface area on the HER

To study the effect of high surface area on the intrinsic activity of Ni_2P catalysts and subsequently to select a catalyst for the CO_2RR, we first evaluated the three catalysts for the HER in 0.5 M H_2SO_4 solution. For this comparison, a pressed pellet electrode configuration was preferred over the electrodes prepared by air brushing of inks or drop-casting the active catalyst on to the conductive support, due to its higher mechanical stability and reproducible results at various current densities. The addition of Nafion improved the proton conduction to the catalyst surface and provided better mechanical stability during $H_2(g)$ generation at high current densities. Fig. 2a illustrates the *iR*-compensated polarization curves of different Ni_2P catalysts. As shown, the cathodic current at any given potential for Ni_2P-CTAB is significantly higher compared to that of SMDP, and SSS. Steady-state activity and electrode degradation (dissolution of the active material in the solution) were investigated by chronopotentiometric (CP) electrolysis at −10 mA cm^{-2} and ICP-OES, respectively. Fig. 2b shows the time dependence of the CP potential of unconditioned pellet electrodes. All the Ni_2P catalysts exhibit an initial activation period (t < 2–3 h), after which there is no considerable change in catalytic activity as observed throughout the CP measurement study. Pre-activation was previously shown to arise from the reduction of surface phosphorus oxides and nickel oxides present on the catalysts which dissolve in the acidic solution, as evidenced by XPS (Fig. S1†).[19] Table S1† illustrates the percentage of Ni leached in the solution as studied by ICP-OES over the 16 h of CP electrolysis. These results show that Ni_2P catalysts can be used for longer durations as an infinitesimal amount (<0.3%) of Ni leaches into the catalytic solution without significant loss of activity or structural stability. The amount of Ni that leaches is consistent with the surface oxides that get reduced and occurs on the first pass only.[19] A lower amount of Ni leaches (<0.02%) for the SSS catalyst which can be attributed to its lower surface area.

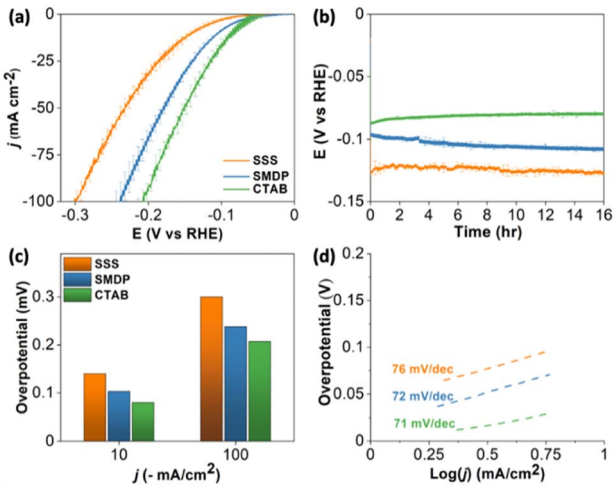

Fig. 2 Electrochemical analyses of the three Ni_2P catalysts under HER conditions at ambient pressure and temperature in 0.5 M H_2SO_4 solution (pH 0). The working compartment was purged with 1 atm. H_2 prior to and during the measurements. (a) Voltammetry at 1 mV s^{-1}, (b) chronopotentiometry analysis at −10 mA cm^{-2}, (c) overpotential values measured at −10 and −100 mA cm^{-2}, and (d) Tafel slopes measured below 0.75 mA cm^{-2}.

To confirm that the observed HER activity is due to the Ni_2P catalyst, rather than any potential contaminant from epoxy or silver used during electrode fabrication, SEM-EDS analysis was performed on the spent electrode. As seen in Fig. S2,† in addition to the aluminum peak arising from the SEM holder, only elemental Ni and P peaks are observed. The HER overpotential of Ni_2P-CTAB is 80 mV at a current density of 10 mA cm^{-2}, which is lower than those of SMDP (103 mV) and SSS (140 mV). Noting that the amount of cathodic current density is proportional to the amount of hydrogen evolved, Fig. 2c summarizes the overpotentials of the three Ni_2P catalysts at 100 mA cm^{-2} (210, 240, and 300 mV, respectively). Tafel slopes were further determined at low current densities below the onset of diffusion limitations (Fig. 2d). Tafel slopes are comparable for all three catalysts at 71, 72 and 76 mV dec^{-1} for Ni_2P-CTAB, -SMDP and -SSS catalysts, respectively. Similar Tafel slopes for the Ni_2P phase have been reported previously.[33,34] These results highlight that the soft-templating strategy with CTAB as the surfactant molecule produces the Ni_2P catalyst that achieves significantly lower overpotentials at commercially useful current densities. Accordingly, we focused on Ni_2P-CTAB for further CO_2RR studies.

Batch cell electrocatalysis

For comparison with historical data,[18] we used a planar cathode geometry in a custom-made batch cell at low current densities

where CO_2 transport is not current limiting. Detailed description of the batch cell reactor suitable for low current densities and small volumes (8 mL) can be found elsewhere.[18] 0.5 M $KHCO_3$ was used as the electrolyte for these studies as it acts as pH buffer during the catalysis as well as a proton donor. As can be seen from Fig. 3a, the total current density (CO_2RR + HER) increases from 0 to −0.3 V *vs.* RHE for both ionomers (average slope = 14 mA V^{-1}). The Nafion ionomer achieves slightly larger total current density than the PFAEM ionomer, although both are below 5 mA cm^{-2}. This compares to a total current density of 0.25 mA cm^{-2} that we previously reported using a similar Ni_2P-SSS preparation in the same ionomer (Nafion), buffer and pH.[18] This 20-fold improvement in current density at 0 V *vs.* RHE is attributed to the high surface area Ni_2P-CTAB catalyst compared to the non-porous SSS catalyst. The corresponding FE (Fig. 3b) shows that essentially all current goes into CO_2RR products using the Ni_2P-CTAB catalyst with methylglyoxal attaining 97% in the PFAEM ionomer and 85% in the Nafion ionomer at 0 V *vs.* RHE. Formic acid and 2,3-furandiol were the other liquid products formed, though their combined FE never exceeded 5% at any potential (Fig. 3b). Identification and quantification of carbon products was done by two methods:[18] from retention times and integration of LC peaks (Fig. S3† shows the representative chromatograph for a CO_2RR sample) and from ^{1}H NMR chemical shifts and multiplet-splittings (Fig. S4†). In conclusion, the increased surface area of Ni_2P-CTAB enables a >20-fold increase in current density into CO_2RR products over the HER, while improving the carbon selectivity into methylglyoxal (max. 97%) *vs.* the equivalent Ni_2P-SSS catalyst possessing 260 times lower BET surface area. The TOF of the major product, methylglyoxal, was calculated by taking the ratio of the moles of methylglyoxal formed during 16 h to the number of sites (see the ESI for the calculation†). Notably, Ni_2P-CTAB (TOF = 618 s^{-1}) showed 22 times higher activity than Ni_2P-SSS (TOF = 48.8 s^{-1}) measured under the same conditions in the batch cell at 0 V *vs.* RHE using the Nafion ionomer. This TOF is even 3 times higher than that of NiP_2-SSS (TOF = 204 s^{-1}) under other conditions, reported previously.[18] The origin of the enhanced C-selectivity towards the methylglyoxal *vs.* furandiol products relative to the batch cell design may be associated with a change in the exposed crystal facets of Ni_2P-CTAB. This question was not addressed further.

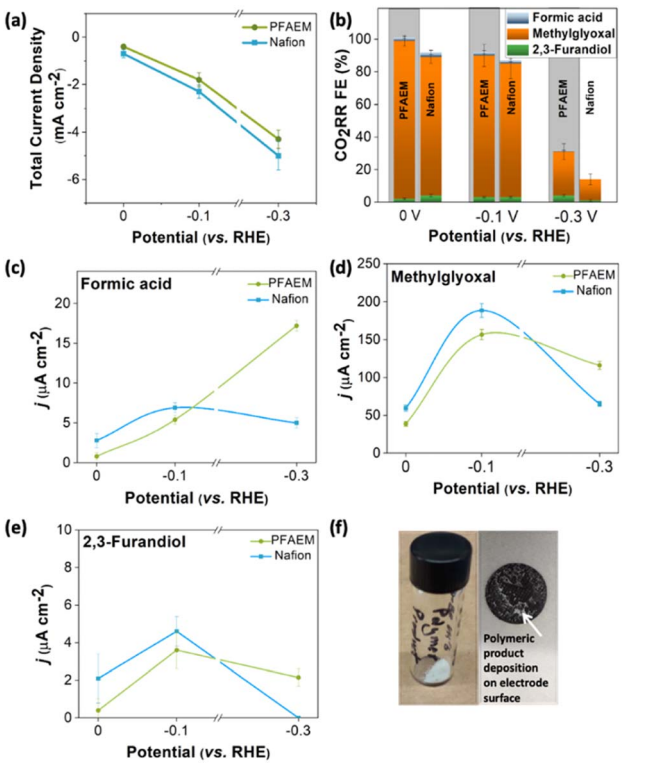

Fig. 3 Electrolysis in the batch reactor using a pressed pellet of the ionomer plus Ni_2P-CTAB catalyst measured in 0.5 M $KHCO_3$ (pH = 7.5) with CO_2 bubbling: (a) total current density, and (b) faradaic efficiency of the Ni_2P-CTAB catalyst with PFAEM (grey shaded) and Nafion as the ionomers at various potentials. Partial current densities (PFAEM = green and Nafion = blue) for (c) formic acid, (d) methylglyoxal, and (e) 2,3-furandiol at various potentials. (f) A solid white polymer product is deposited on the cathode at 100 mA cm^{-2} in the batch cell (see the inset).

At potentials 0, −0.1 and −0.3 V *vs.* RHE, a higher FE to CO_2RR products is observed using the PFAEM ionomer than using the Nafion ionomer (Fig. 3b). For the methylglyoxal product these are 97%, 85% and 25%, respectively. As the potential increases more negative than −0.1 V, the HER increases substantially although less HER occurs with PFAEM than with Nafion, as expected. This relative shift to the HER at higher current density is due to an increase in the local pH which results in conversion of locally dissolved CO_2 at the electrode surface to the unreactive bicarbonate form (*vide supra*). This agrees with our earlier results on Ni_2P-SSS where even at lower current densities the HER takes over the CO_2RR in buffered bicarbonate electrolyte on all five Ni_xP_y catalysts.[18] This interpretation of the consequence of the shift to the HER on the CO_2RR rate is also seen in the partial current densities for the three major CO_2RR products shown in Fig. 3c (formic acid), Fig. 3d (methylglyoxal) and Fig. 3e (2,3-furandiol). Here we see that the PFAEM ionomer overtakes Nafion as the preferred ionomer for all three products at potentials more negative than −0.1 V where the HER increases rapidly. Notably, when Ni_2P-CTAB with the Nafion ionomer as the binder is evaluated in the batch cell reactor at 100 mA cm^{-2}, we observe the deposition of a white polymeric product on the cathode (Fig. 3f). The H_2 FE is found to be 94% while the only liquid product, methylglyoxal has a 2% FE (Fig. S5†). Hence, the remaining FE (4%) was attributed to polymer formation. The obtained polymer was isolated and is discussed in the next section. The FTIR spectrum and functional group assignments are depicted in Fig. 5.

Flow-cell electrocatalysis

The CO_2RR performance in stirred batch reactors at applied potentials close to the RHE is intrinsically low, while at higher applied potentials $CO_{2(aq)}$ transport through the electrolyte becomes rate-limiting and favors the HER. Hence, to fully take advantage of the 260-times higher BET surface area and to overcome the limitations of the batch reactor, we examined the

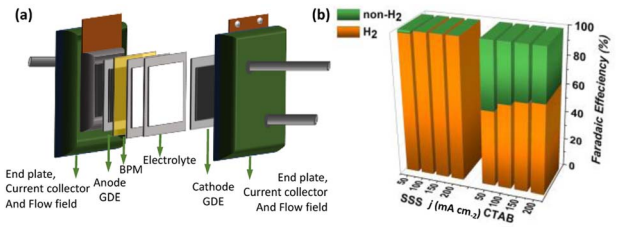

Fig. 4 (a) Electrolysis in a flow-cell using the GDE design. (b) The FE for the CO_2RR and HER on both Ni_2P-SSS and Ni_2P-CTAB in the flow cell (catalyst loading 0.5 mg cm^{-2}, PFAEM binder, catholyte 0.4 M K_2SO_4).

performance of Ni_2P catalysts supported on a GDE in a flow-cell design. The flow-cell reactor design (Fig. 4a) has been previously described in detail by Chen *et al.*[24] A bipolar membrane (BPM) was used in all the flow cell experiments to prevent the CO_2RR product crossover and to enable the use of separate electrolytes for the anode and cathode. In addition, we also anticipated to perform future reactions at different pH in which utilization of a BPM will be beneficial. The flow setup uses an aqueous electrolyte layer between the cation exchange layer of the membrane and the cathode. The cathode flow-field is composed of K_2SO_4 electrolyte with CO_2 gas flowing into the backside of the porous gas diffusion layer at a rate of 2 L min^{-1}. It is opposed by back pressure from the catholyte on the membrane side of the GDE. This flow field creates a gas–liquid–solid zone within the GDE that ideally brings CO_2 gas, water and aqueous protons (from the anode) to react together at the catalyst/ionomer interface. If this interface gets flooded with liquid electrolyte it will slow the delivery of $CO_{2(aq)}$ to the catalyst at high current densities and possibly limit the CO_2RR current. If protons are blocked from reaching the catalyst, then the reactive hydrides that must form on the catalyst surface will be produced from reduction of water. The latter reaction produces hydroxide at the catalyst surface and reacts with $CO_{2(aq)}$ to form inactive bicarbonate, resulting in possible loss of CO_2RR performance. In several cases, high CO_2 reactivity has been observed under alkaline conditions when CO_2 mass transport and dissolution at the electrode surface $(CO_2)_{aq}$ are both fully realized.[35–37] Although, if these conditions are not met then high alkalinity created at high current density lowers the available CO_2 by forming inactive bicarbonate.[38] To avoid flooding of the GDL-catalyst layer and the resulting loss of CO_2RR current, several criteria need to be considered to balance the capillary force controlling the transport of liquid electrolyte from one side, and the CO_2 gas pressure controlling the concentration of dissolved $(CO_2)_{aq}$ from the backside.[39] Accordingly, the performance of this flow-cell design depends on several other factors than the reactor design described above.

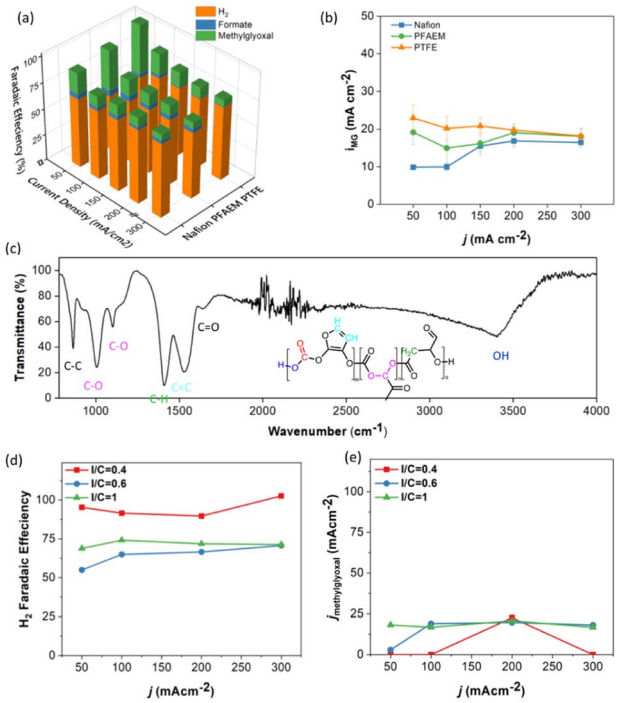

Fig. 5 (a) Faradaic efficiency for the CO_2RR products produced in the flow cell as a function of current density and type of binder used. The remaining faradaic efficiency is for the polymeric product formed (omitted for clarity). (b) Partial current density for methylglyoxal (major product) at various current densities and (c) ATR-FTIR spectrum of the polymeric product formed during the CO_2RR on Ni_2P catalysts. Functional group assignments are indicated based on the infrared database. (d) H_2 faradaic efficiencies and (e) methylglyoxal partial current density at various total current densities for different catalyst–ionomer ratios.

The Ni_2P-SSS catalyst produces CO_2RR products only at low current densities; the total carbon product FE = 2% at 50 mA cm^{-2} (Fig. 4b), while at more negative potentials the current arises exclusively from hydrogen (>50 to 200 mA cm^{-2}). By contrast, the Ni_2P-CTAB catalyst prepared with the same ionomer produces significantly more CO_2RR products over the entire range of currents from 50 to 200 mA cm^{-2} and FE = 40–50%. The cell potentials needed to achieve these higher currents ranged from 3.06 V to 4.25 V. These results imply that CO_2 mass transport may limit the current density above 50 mA cm^{-2} when using the low surface area, non-porous, SSS catalyst. Durability under electrolysis conditions is a shortcoming of all MEA-based CO_2 reduction demonstrations. However, the field has been making good progress in extending operational lifetimes. This same flow cell was used in an earlier report of formic acid production where initial durability was demonstrated for 11 hours,[24] and more recently, 24 hours of continuous operation has been achieved with moderate performance loss.[40] There is still a long way to go to realize the thousands of operational hours needed to be industrially relevant, but there is no known fundamental degradation mechanism that would prevent making progress toward this target through continued research and development.

Choice of ionomer–binder

We further optimized the choice of binder/ionomer within the GDE which determines the location and reactant accessibility at the gas–liquid–solid interface using the Ni_2P-CTAB catalyst. We examined a proton-conducting cationic ionomer (Nafion),

a hydroxide-conducting anionic ionomer (PFAEM) and a neutral polymer binder (PTFE). The flow cell configuration produces significantly higher total current densities for all ionomer/binder combinations, between 50 and 300 mA cm^{-2}, compared to the batch reactor (<5 mA cm^{-2}) (Fig. 5). Analogous to the batch reactor, PFAEM achieves slightly higher performance compared to Nafion, while the neutral binder PTFE is intermediate between them (Fig. S6† highlights H_2 FE at various current densities with different binders). The total CO_2RR product FE using PFAEM changes relatively little between 50 mA cm^{-2} (47%) and 300 mA cm^{-2} (36%), indicating relatively stable CO_2RR production over this wide range (details in Table S2†). This FE corresponds to an almost 60-fold increase in current density over the batch reactor (30% FE to methylglyoxal at 5 mA cm^{-2} total current, Fig. 3). The superior performance of PFAEM as the binder is consistent with the batch reactor results and we interpret it the same way; PFAEM lowers the alkalinity at the cathode surface caused by the HER, thus suppressing CO_2 hydrolysis by OH^- and leaving CO_2 available for reduction. The excellent performance of PTFE as the non-ionic binder in the GDE is ascribed to its hydrophobic properties, which we postulate serves to maintain the gas–liquid–solid interface needed for efficient CO_2 delivery to the catalyst.

Fig. 5a plots the FE for H_2, formate and methylglyoxal, the major soluble products, as a function of the current densities and different binders. Although identical products are formed in the two cells, the product distribution differs in the batch cell and flow cell using the same Ni_2P-CTAB catalyst. In the batch cell, we observed that the CO_2RR yield is close to 100% FE when operating near the thermodynamic potential for the CO_2RR. In contrast to the batch cell results, methylglyoxal was found to be the dominant CO_2 product under all conditions in the flow reactor. The reason for this high selectivity towards methylglyoxal is postulated to be due the high energy barrier for conversion of methylglyoxal to the 2,3-furandiol product – two large endergonic barriers for keto-enolization steps were previously estimated (41.8 and 28.0 kJ mol^{-1}).[18] At current densities below 150 mA cm^{-2}, a marked difference in the partial current density to methylglyoxal was observed for the three ionomers (Fig. 5b). PTFE maintained constantly high selectivity towards the formation of methylglyoxal ($j = 24$ mA cm^{-2}) at all examined total current densities, more than that of PFAEM ($j = 19$ mA cm^{-2}) and Nafion ($j = 9$ mA cm^{-2}). The first two ionomers achieved constant partial current densities of about 18 mA cm^{-2} up to 300 mA cm^{-2}. In the case of Nafion, an increase in the partial current density occurs above 100 mA cm^{-2}, above which all three ionomers exhibit comparable partial current densities. The missing FE in Fig. 5a is attributed to the formation of the same insoluble polymer that is observed in the batch cell experiments done at 100 mA cm^{-2} (Fig. 3f). Due to its precipitation inside the GDE, the continuous stream of flowing electrolyte and the larger volume, the amount of the insoluble polymer was difficult to quantify. We isolated the water-insoluble solid white product from the batch cell experiment and washed multiples times with water to remove any adsorbed impurities. When investigated using attenuated total reflection-Fourier transform infrared spectroscopy (ATR-FTIR, Fig. 5c) in the frequency range (800–4000 cm^{-1}), the spectrum of the isolated solid polymer exhibited strong peaks at 864 cm^{-1} ($(CH_2)_n$ stretch), 1005 cm^{-1} (C–O stretch ether), 1100 cm^{-1} (C–O stretch ether), 1408 cm^{-1} (C–H stretch), 1530 cm^{-1} (CC stretch) and 3400 cm^{-1} (OH stretch). The peak positions observed for the entire range are available in Table S3.† The frequencies and intensities were used to assign the functional groups (from the ATR-IR polymer database on the know-it-all software) that are present and from this we provide an approximate composition of the solid polymer. We attribute the formation of the polymeric product at high currents to the esterification of the hydroxyl groups of 2,3-furandiol with CO_2, as well as the base-catalyzed condensation of methylglyoxal with CO_2. The molecular weight increases with increasing negative bias and time of reaction. Further analysis of the resulting polycarbonate product is underway and will be characterized for average mass and other physicochemical properties in the future. Attempts at redissolution of the polymer in acid or alkali were not successful.

To determine the optimal ionomer to catalyst concentration ratio (I/C), which is a significant performance determining factor for the electrocatalytic CO_2RR, we compared the PTFE to Ni_2P-CTAB ratio between 0.4 and 1. Fig. 5d and e plots the H_2 FE and methylglyoxal partial current density at various current densities. A low I/C ratio of 0.4 was found to favor the HER at current densities ranging from 50 to 300 mA cm^{-2}. On the other hand, increasing the I/C ratio to 0.6 and 1 led to almost 32 and 43% CO_2RR products at 50 mA cm^{-2} which gradually decreased to 28% at 300 mA cm^{-2} in both the cases. We note that based on these results with increasing PTFE content in the GDE, there is suppression of the HER that can be attributed to increased CO_2 accessibility to active sites of Ni_2P-CTAB. Thus, there exists an optimal ratio of ionomer to catalyst that facilitates CO_2 access to the catalyst and sufficient water at the same time.[27]

Conclusions

By comparing electrocatalytic performance of a single pure phase Ni_2P compound prepared using three methods to modify the surface area to volume ratio, it was found that significantly improved CO_2RR current densities and selectivity *vs.* H_2 production could be achieved using the Ni_2P-CTAB catalyst prepared by a low-temperature soft-templating method. This high surface area catalyst permits use of a flow cell configuration with high CO_2 delivery rate that achieves constant CO_2RR yields across a wide range of currents and with high product selectivity towards a single product methylglyoxal, in contrast to the non-porous Ni_2P-SSS catalyst. The influence of anionic *vs.* cationic *vs.* neutral binders revealed that the proton conducting ionomer was found to predominantly favor the HER, while the anionic ionomer maintains high C/H selectivity at all current densities while suppressing the HER. The combination of the high surface area Ni_2P electrocatalyst with an anionic ionomer results in continuous CO_2 conversion to a single soluble C_3 product (methylglyoxal) in yields that are the highest in the literature. As the product concentration increases further at high current density, a solid polycarbonate polymer forms that

is composed of the condensation of the soluble monomers with CO_2. Finally, we believe that this work will motivate future development in the field of CO_2 conversion by electrocatalysis to produce sustainable products and further expand this promising technology.

Conflicts of interest

The authors declare no competing financial interest.

Acknowledgements

This research was funded by the Dept of Energy EERE divisions through an NREL internal LDRP proposal. This work was authored in part by the National Renewable Energy Laboratory, operated by Alliance for Sustainable Energy, LLC, for the U.S. Department of Energy under Contract Number DE-AC36-08GO28308. Funding was provided by the U.S. Department of Energy, Office of Energy Efficiency and Renewable Energy, Hydrogen and Fuel Cell Technologies Office. The views expressed in the article do not necessarily represent the views of the DOE or the U.S. Government. The U.S. Government retains and the publisher, by accepting the article for publication, acknowledges that the U.S. Government retains a nonexclusive, paid-up, irrevocable, worldwide license to publish or reproduce the published form of this work, or allow others to do so, for U.S. Government purposes.

Notes and references

1 S. M. Jordaan and C. Wang, *Nat. Catal.*, 2021, **4**, 915–920.
2 M. C. O. Monteiro, M. F. Philips, K. J. P. Schouten and M. T. M. Koper, *Nat. Commun.*, 2021, **12**, 4943.
3 D. Gao, H. Zhou, J. Wang, S. Miao, F. Yang, G. Wang, J. Wang and X. Bao, *J. Am. Chem. Soc.*, 2015, **137**, 4288–4291.
4 M. Liu, Y. Pang, B. Zhang, P. De Luna, O. Voznyy, J. Xu, X. Zheng, C. T. Dinh, F. Fan, C. Cao, F. P. G. de Arquer, T. S. Safaei, A. Mepham, A. Klinkova, E. Kumacheva, T. Filleter, D. Sinton, S. O. Kelley and E. H. Sargent, *Nature*, 2016, **537**, 382–386.
5 S. Liu, H. Tao, L. Zeng, Q. Liu, Z. Xu, Q. Liu and J. L. Luo, *J. Am. Chem. Soc.*, 2017, **139**, 2160–2163.
6 Y. Wang, P. Han, X. Lv, L. Zhang and G. Zheng, *Joule*, 2018, **2**, 2551–2582.
7 J. Medina-Ramos, J. L. DiMeglio and J. Rosenthal, *J. Am. Chem. Soc.*, 2014, **136**, 8361–8367.
8 J. Yu, J. Wang, Y. Ma, J. Zhou, Y. Wang, P. Lu, J. Yin, R. Ye, Z. Zhu and Z. Fan, *Adv. Funct. Mater.*, 2021, **31**, 2102151.
9 J. T. Feaster, C. Shi, E. R. Cave, T. Hatsukade, D. N. Abram, K. P. Kuhl, C. Hahn, J. K. Nørskov and T. F. Jaramillo, *ACS Catal.*, 2017, **7**, 4822–4827.
10 Z. Chen, G. Zhang, Y. Wen, N. Chen, W. Chen, T. Regier, J. Dynes, Y. Zheng and S. Sun, *Nano-Micro Lett.*, 2021, **14**, 25.
11 Z. Yin, C. Yu, Z. Zhao, X. Guo, M. Shen, N. Li, M. Muzzio, J. Li, H. Liu, H. Lin, J. Yin, G. Lu, D. Su and S. Sun, *Nano Lett.*, 2019, **19**, 8658–8663.
12 J. Huang, M. Mensi, E. Oveisi, V. Mantella and R. Buonsanti, *J. Am. Chem. Soc.*, 2019, **141**, 2490–2499.
13 L. Xie, J. Liang, C. Priest, T. Wang, D. Ding, G. Wu and Q. Li, *Chem. Commun.*, 2021, **57**, 1839–1854.
14 R. Kortlever, I. Peters, C. Balemans, R. Kas, Y. Kwon, G. Mul and M. T. Koper, *Chem. Commun.*, 2016, **52**, 10229–10232.
15 Y. Zhou, F. Che, M. Liu, C. Zou, Z. Liang, P. De Luna, H. Yuan, J. Li, Z. Wang, H. Xie, H. Li, P. Chen, E. Bladt, R. Quintero-Bermudez, T. K. Sham, S. Bals, J. Hofkens, D. Sinton, G. Chen and E. H. Sargent, *Nat. Chem.*, 2018, **10**, 974–980.
16 N. S. Romero Cuellar, C. Scherer, B. Kaçkar, W. Eisenreich, C. Huber, K. Wiesner-Fleischer, M. Fleischer and O. Hinrichsen, *J. CO_2 Util.*, 2020, **36**, 263–275.
17 K. U. D. Calvinho, A. W. Alherz, K. M. K. Yap, A. B. Laursen, S. Hwang, Z. J. L. Bare, Z. Clifford, C. B. Musgrave and G. C. Dismukes, *J. Am. Chem. Soc.*, 2021, **143**, 21275–21285.
18 K. U. D. Calvinho, A. B. Laursen, K. M. K. Yap, T. A. Goetjen, S. Hwang, N. Murali, B. Mejia-Sosa, A. Lubarski, K. M. Teeluck, E. S. Hall, E. Garfunkel, M. Greenblatt and G. C. Dismukes, *Energy Environ. Sci.*, 2018, **11**, 2550–2559.
19 A. B. Laursen, K. R. Patraju, M. J. Whitaker, M. Retuerto, T. Sarkar, N. Yao, K. V. Ramanujachary, M. Greenblatt and G. C. Dismukes, *Energy Environ. Sci.*, 2015, **8**, 1027–1034.
20 A. B. Laursen, R. B. Wexler, M. J. Whitaker, E. J. Izett, K. U. D. Calvinho, S. Hwang, R. Rucker, H. Wang, J. Li, E. Garfunkel, M. Greenblatt, A. M. Rappe and G. C. Dismukes, *ACS Catal.*, 2018, **8**, 4408–4419.
21 R. B. Wexler, J. M. P. Martirez and A. M. Rappe, *Chem. Mater.*, 2016, **28**, 5365–5372.
22 R. B. Wexler, J. M. P. Martirez and A. M. Rappe, *ACS Catal.*, 2017, **7**, 7718–7725.
23 P. Liu and J. A. Rodriguez, *J. Am. Chem. Soc.*, 2005, **127**, 14871–14878.
24 Y. Chen, A. Vise, W. E. Klein, F. C. Cetinbas, D. J. Myers, W. A. Smith, T. G. Deutsch and K. C. Neyerlin, *ACS Energy Lett.*, 2020, **5**, 1825–1833.
25 R. Nagarajan, *Langmuir*, 2002, **18**, 1–38.
26 P. Ekwall, L. Mandell and P. Solyom, *Colloids Interface Sci.*, 1971, **35**, 266–272.
27 S.-C. Chien, G. Pérez-Sánchez, J. R. B. Gomes, M. N. D. S. Cordeiro, M. Jorge, S. M. Auerbach and P. A. Monson, *J. Phys. Chem. C*, 2017, **121**, 4564–4575.
28 Q. Li and X. Hu, *Phys. Rev. B: Condens. Matter Mater. Phys.*, 2006, **74**, 035414.
29 A. B. Hernandez, H. Ariga, S. Takakusagi, K. Kinoshita, S. Suzuki, S. Otani, S. T. Oyama and K. Asakura, *Chem. Phys. Lett.*, 2011, **513**, 48–52.
30 K. Edamoto, *Appl. Surf. Sci.*, 2013, **269**, 7–11.
31 H. Ariga, M. Kawashima, S. Takakusagi and K. Asakura, *Chem. Lett.*, 2013, **42**, 1481–1483.
32 W. Papawassiliou, J. P. Carvalho, N. Panopoulos, Y. Al Wahedi, V. K. S. Wadi, X. Lu, K. Polychronopoulou, J. B. Lee, S. Lee, C. Y. Kim, H. J. Kim, M. Katsiotis, V. Tzitzios, M. Karagianni, M. Fardis, G. Papavassiliou and A. J. Pell, *Nat. Commun.*, 2021, **12**, 4334.

33 J.-S. Moon, J.-H. Jang, E.-G. Kim, Y.-H. Chung, S. J. Yoo and Y.-K. Lee, *J. Catal.*, 2015, **326**, 92–99.
34 S. Huo, S. Yang, Q. Niu, F. Yang and L. Song, *Int. J. Hydrogen Energy*, 2020, **45**, 4015–4025.
35 C.-T. Dinh, F. P. García de Arquer, D. Sinton and E. H. Sargent, *ACS Energy Lett.*, 2018, **3**, 2835–2840.
36 C. M. Gabardo, C. P. O'Brien, J. P. Edwards, C. McCallum, Y. Xu, C.-T. Dinh, J. Li, E. H. Sargent and D. Sinton, *Joule*, 2019, **3**, 2777–2791.
37 I. Grigioni, L. K. Sagar, Y. C. Li, G. Lee, Y. Yan, K. Bertens, R. K. Miao, X. Wang, J. Abed, D. H. Won, F. P. García de Arquer, A. H. Ip, D. Sinton and E. H. Sargent, *ACS Energy Lett.*, 2020, **6**, 79–84.
38 J. E. Huang, F. Li, A. Ozden, A. S. Rasouli, F. P. Garcia de Arquer, S. Liu, S. Zhang, M. Luo, X. Wang, Y. Lum, Y. Xu, K. Bertens, R. K. Miao, C. T. Dinh, D. Sinton and E. H. Sargent, *Science*, 2021, **372**, 1074–1078.
39 A. Hodges, A. L. Hoang, G. Tsekouras, K. Wagner, C. Y. Lee, G. F. Swiegers and G. G. Wallace, *Nat. Commun.*, 2022, **13**, 1304.
40 T. D. Nguyen-Phan, L. Hu, B. H. Howard, W. Xu, E. Stavitski, D. Leshchev, A. Rothenberger, K. C. Neyerlin and D. R. Kauffman, *Sci. Rep.*, 2022, **12**, 8420.